Publication Year	2020
Acceptance in OA	2025-02-13T10:45:37Z
Title	The Philae lander reveals low-strength primitive ice inside cometary boulders
Authors	O'Rourke, Larry, Heinisch, P., Blum, J., Fornasier, S., FILACCHIONE, GIANRICO, Van Hoang, H., CIARNIELLO, Mauro, RAPONI, Andrea, Gundlach, B., Blasco, R.A., Grieger, B., Glassmeier, K.-H., Küppers, M., Rotundi, Alessandra, Groussin, O., Bockelée-Morvan, D., Auster, H.-U., Oklay, N., Paar, G., Perucha, M.P.C., Kovacs, G., Jorda, L., Vincent, J.-B., CAPACCIONI, FABRIZIO, Biver, N., Parker, J.W., Tubiana, C., Sierks, H.
Publisher's version (DOI)	10.1038/s41586-020-2834-3
Handle	http://hdl.handle.net/20.500.12386/35930
Journal	NATURE
Volume	586

ABSTRACT

The Philae lander reveals low strength primitive ice inside cometary boulders

On the 12th November 2014, the Philae lander descended towards comet 67P/Churyumov-Gerasimenko colliding once and rebounding twice off the surface before arriving at its final location in the Abydos region. The landing process provided new insights on the properties of a cometary nucleus[1,2,3]. Here we report on the previously undiscovered second touchdown site where Philae spent nearly 2 full minutes making four distinct surface contacts on two adjoining cometary boulders. While travelling through the crevice between the boulders, it exposed water ice in their interiors. Our multi-instrument observations find this highly unprocessed water ice mixed with ubiquitous dark organic-rich material has a local volume dust/ice ratio of approximately 1.2:1 matching values previously found in newly exposed water ice linked to an outburst[4] and water ice observed in shadow[5,6]. At the end of the crevice, Philae made a deep angular impression in the boulder's ice providing in-situ measurements confirming primitive ice has a very low compressive strength (< 12Pa) as well as allowing a key estimation (75 ± 7%) to be made for the porosity of the boulders' icy interiors. Our results provide important constraints for spacecraft missions wishing to retrieve samples from the interior of cometary boulders.

MAIN TEXT

Flybys and rendezvous missions have been key to providing close up images of cometary surface structures delivering important insights into the chemical and physical processes that have defined them. The presence of boulders on their surfaces with sizes ranging from the metre scale up to 10s of metres often in locations not matching where they were initially exposed certainly points to the dynamic nature of their creation. A determination of mechanical strength properties derived from in-situ measurements carried out on the primitive ice located in the interior of a cometary boulder allows unique comparisons to be made with the cometary body internal structure, provides insights on its dynamical history and delivers important constraints for spacecraft intending to land on their surface to drill into their interior or indeed to retrieve samples.

The European Space Agency's Rosetta mission[14] was launched in 2004 and began orbiting comet 67P/Churyumov-Gerasimenko in August 2014. On 12th November 2014 the Philae lander was released with faulty harpoons, touching down on the surface on two clear occasions while also experiencing a glancing collision against the Hatmehit depression edge. After touchdown 2, it proceeded to its final landing position located under an overhang in the Abydos region of the comet[1] (see Fig. 1a-d). While scientific analysis of data[1,2,15] from Philae's first and third touchdown points have led to a significant step in understanding the properties of a cometary nucleus, the location and scientific implications stemming from the second touchdown point were unknown up to now. Its importance was noted[16] however as Philae was found to have changed both velocity and rotation rate at this location as well as penetrated the surface with the Rosetta

Lander Magnetometer and Plasma Monitor[17] (ROMAP) sensor, possibly exposing ice at the same time.

The production of a new Philae landing trajectory (Supplementary Methods) served to kick-off the search for the touchdown 2 point with a ridge region identified as being a likely candidate for its location[15]. A comparative analysis was performed of this area using pre- and post-landing imagery from the ROSETTA Optical, Spectroscopic, and Infrared Remote Imaging System (OSIRIS) [18] combined with high resolution digital terrain models of the ridge and the Abydos region as a whole. While significant changes in boulder positions were observed in the Abydos valley (Supplementary Fig. 7e and f), the geomorphological structures along the length of the ridge showed no differences with regards to position or orientation. Changes were found however in the pre- and post-landing surface morphology of two adjoining boulders located on the ridge (Extended data Fig. 1 & Fig. 2, Supplementary Fig. 8). These changes included the identification of an unusual ice feature located in the boundary between them (Fig. 1e, 1f, Supplementary Fig. 2 Animation). Our analysis of these changes found that only Philae's presence could explain their existence (Supplementary Methods). As the topological structures of these two boulders, viewed from above, give the impression of a skull face as shown in Supplementary Fig. 6, we chose to name the location as skull-top ridge and the boundary between the two boulders as skull-top crevice. We highlight in Methods that the boulders' themselves represent assemblages of dust/ice aggregates.

The timing involved in this chain of events [Extended Data Table 1, Supplementary Fig. 1 animation] was derived from magnetometer data produced by the ROMAP sensor and checked against thermal & power information from Philae's

subsystems. The ROMAP instrument provided attitude information (combined with the Rosetta Plasma Consortium Fluxgate Magnetometer (RPC-MAG)[19]) as well as unique accelerometer measurements based upon sensor boom movement. Combined with our image analysis, a reassessment of the ROMAP science data (see Methods and Supplementary Methods determined that the initial contact took place at 17:23:48±10s, approximately 1.5 minutes before the previously published contact time[20]. Indeed Philae spent nearly two full minutes at Touchdown 2 (TD2) making four surface contacts during this time. Of the four, the third (TD2c) of these contacts (Fig. 2) is the most significant due to the deep depression visible in an ice-like feature on the side of a crevice. We found a perfect correlation between the ROMAP boom movements beginning at 17:25:24 (Fig. 2a) and the expected reaction of that boom upon compressing/stamping the ice-like feature in the crevice (Fig. 2b and c). The compression lasted 3 seconds before Philae proceeded to rise out of the crevice to then make its final TD2 contact with the surface creating the eye of the skull in the process.

Data from the OSIRIS and VIRTIS instruments on the Rosetta orbiter were used to determine whether the high albedo ice-like features observed in the skull-top crevice were water ice. For the OSIRIS instrument, we focussed on multi-filter images generated during the timeframe of 12th to 14th June 2016 (Fig. 3a, Extended Data Fig. 3). A spectrophotometric analysis of the datasets from this period (see Methods) provided spatially resolved data that confirmed the presence of water ice in the crevice, matching a visible area of approximately 3.5 m^2, with a brightness 6 times greater than the dust covered terrain. The water ice abundance was derived from the observed reflectance, after corrections were made for the illumination conditions and phase function based upon geographical mixtures of the comet dark terrain and water ice (grain size of 30-100

microns) applied to the bright material absolute reflectance. A water ice abundance value of 46.4% +/- 2% was measured during the 14th June 2016 10:30 observations (Fig. 3c & d, Extended Data Table 1), resulting in an approximate local volume dust/ice ratio of 1.2:1. Assuming a dust/ice bulk density ratio of two[21], and a similar porosity for dust and ice material, the local dust/ice mass ratio is approximately 2.4. This value is below the average dust/ice mass ratio for the nucleus[22] which lies between 3 and 9 and can be explained[29] using a gas activity model which finds that the pristine ice can exist locally in values < 5 for at most 5% of the volume of the nucleus.

A less sensitive result using data from the VIRTIS Instrument on the 14th June 2016 confirmed this detection of water ice. Fig. 3b shows the resulting hyperspectral image of the Abydos region with the skull-face crevice identified at the edge of the field of view. A signal from the ice located in the crevice was found in the tail of the optical point spread function (see Methods). An estimation by VIRTIS of the water ice abundance in the location concurred with that of the OSIRIS measurement whereby the water ice rich spot was determined to have an approximate area of 1.27 m^2 (matching the upper bound of 48% of 3.5m^2) calculated from the inferred abundances (0.5% over an area of 253m^2).

The general longevity of ice on the comet surface is dependent on local surface topography[6,23,24,25] with most ice features disappearing quite quickly due to limited surface shading from the sun within days to weeks of discovery. Local dust/ice ratios < 1.5:1 equivalent to that in the skull-top crevice have been found at other locations across the comet, in particular in newly exposed water ice observed on cliffs and scarps linked in some cases to outbursts as well as in clustered bright spots in both hemispheres[4,6,23].

These dust/ice values were found to reduce over time due to solar illumination exposure. The fact that the ice in the crevice (Fig. 1, Fig. 2) was observed 22 months after landing without significant measurable changes and that our measurement of high water ice abundance was made 19 months after Philae touched down, both point to the ice in the crevice receiving very low sun illumination due to shadowing.

This very low illumination is supported by our measurements of the crevice dimensions; the width of the specific point where compression took place fully matches the width of the Philae lander thus pointing to very little sublimation or erosion having taken place (Fig. 3e-e1). We found using a horizon mask (Supplementary Fig. 9) that the ice feature in the left hand side of the crevice was illuminated <0.55% of the time during the perihelion passage while the ice on the right hand side of the crevice, where the compression took place, received <0.21% of direct sunlight during the same period (Supplementary Methods). Using as input the corresponding energy flux, our sublimation modelling over-estimates by an order of magnitude the amount of ice that sublimed (than is visible from the imagery) pointing to even greater morphological shadowing than our horizon mask could derive. For these reasons, we conclude that while the super-volatiles may have sublimated over time, the water ice itself has remained stable and can be considered to be in a highly unprocessed state.

The depth of the impression made by Philae in this icy surface combined with a detailed correlation of the ROMAP boom measurements contribute to provide direct in-situ measurements allowing an estimation to be made of the compressive strength of this dust/ice feature. The depth of the impression in the ice is 0.246 ± 0.049 m (Fig. 3e-e2) and its area is 0.2208 m^2 (see methods). A detailed analysis performed and explained in

Methods, finds the compressive strength of the ice to be <12Pa. It is important to flag that this very low compressive strength is the result of compression of primitive ice at the time of the Philae landing itself where it was, up to that point, buried under a thick dust covering.

While compressive strengths[1,2] of 1kPa and 2MPa were measured at Philae's first touchdown and final landing site respectively (although deployment uncertainties do affect the reliability of the MUPUS result), a number of other publications find much lower values. Model dependent analyses of the collapse of cliff overhangs observed from orbit[26] as well as those derived from the scratches Philae made at the final landing location[15] calculated compressive strength values ranging between 30 Pa and 150 Pa for the former and from 10 to 100Pa for the latter. Our in-situ findings are consistent therefore with these model-based derivations.

Three independent porosity estimations have been made for this comet with values ranging from 65-85% (Philae Consert radar) [3 (+NEW)], through 70-75% (Rosetta Radio science Instrument) [27] and a modelled third estimate[28] of 63-79%. These same numbers equate to volume filling factors of 0.15-0.35, 0.25-0.3 and 0.21-0.37 respectively. To derive a porosity value linked to our measurements, we modelled the compression Philae made in the cometary boulder material, with the resulting loss of energy allowing to determine how much the volume-filling factor of the material was altered. The model we use[7] assumes that the material making up the cometary interior is made up of a hierarchical arrangement of building blocks. According to this model, applied for the case of this paper to the interior of a cometary boulder, the sub-µm-sized solid grains (REFS: Mannel et al. 2019, A&A 630, A26; Güttler et al. 2019, A&A 630,

A24) are contained in larger units ("pebbles"), which themselves are clustered together to make up the boulder.

We find in the Methods that such an arrangement of hierarchical building blocks, which previously has demonstrated excellent correlation with the Philae Consert radar results (REF: Herique et al. 2019, A&A 630, A6), also provides the conditions needed to achieve the low compressive strength (<12 Pa) of the material of the boulder into which Philae stamped. As a result, we infer that the ice-containing boulder possesses a volume filling factor of the material of 0.25 ± 0.07, (porosity range of 68-77) equivalent to previously published values for the overall nucleus of comet 67P.

Our results provide important constraints for missions e.g. Comet Nucleus Sample Return, Ambition, among others, whose aim is to retrieve and return to Earth a volatile rich cryogenic sample from the interior of a comet. With our findings suggesting the presence of ice just below the dusty surface of cometary boulders, deep excavating drills are not needed. The softness of the core ice contributes to ease in retrieval and storage processes. The operational dangers of landing in a cometary boulder field will need careful study and preparation however.

REFERENCES

1. Biele, J. et al., The landing(s) of Philae and inferences about comet surface mechanical properties, Science, 349, 6247, 2015.acc
2. Spohn, T. et al., Thermal and mechanical properties of the near-surface layers of comet 67P/Churyumov-Gerasimenko, Science, 349, 6247, 2015
3. Kofman, W., Herique, A., Barbin, Y., et al., Properties of the 67P/Churyumov-Gerasimenko interior revealed by CONSERT radar, Science, 349, 2015
4. Pajola, M. *et al*. The pristine interior of comet 67P revealed by the combined Aswan outburst and cliff collapse. *Nat. Astron*. 1, 0092 2017.
5. Fornasier, S. et al., Surface evolution of the Anhur region on comet 67P/Churyumov-Gerasimenko from high-resolution OSIRIS images, A&A, 630, A13, 2019
6. Oklay, N. et al, Long-term survival of surface water ice on comet 67P, MNRAS 469, S582–S597, 2017
7. Blum, J. et al., Evidence for the formation of comet 67P/Churyumov-Gerasimenko through gravitational collapse of a bound clump of pebbles, MNRAS, 469, S755-S773, 2017.
8. Morbidelli, A., Rickman, H., Comets as collisional fragments of a primordial planetesimal disk, A&A, 583, A43, 2015
9. Blum, J. et al, Comets formed in solar-nebula instabilities! – An experimental and modeling attempt to relate the activity of comets to their formation process, Icarus, 235, 156-169, 2014
10. Skorov, Y.V., Blum, J., Dust release and tensile strength of the non-volatile layer of cometary nuclei. Icarus 221, 1–11, 2012
11. Davidsson, B. J. R. et al., The primordial nucleus of comet 67P/Churyumov-Gerasimenko, A&A 592, 2016
12. Meisner, T., et al., Preplanetary scavengers: Growing tall in dust collisions, A&A, 559, A123, 2013
13. Blum, J. et al, The Physics of Protoplanetesimal Dust Agglomerates. I. Mechanical Properties and Relations to Primitive Bodies in the Solar System, APJ, 652, 2, 1768-1781, 2006

14. Glassmeier, K. *et al.* The Rosetta Mission: Flying Towards the Origin of the Solar System. *Space Sci Rev* 128, 1–21, 2007
15. Heinisch, P. et al., Compressive strength of comet 67P/Churyumov–Gerasimenko derived from Philae surface contacts, A&A, 630, A2, 2019
16. Heinisch, P. et al, Reconstruction of the flight and attitude of Rosetta's lander Philae, Acta Astronautica, 140, 509-516, 2017
17. Auster, H.U., *et al.* ROMAP: Rosetta Magnetometer and Plasma Monitor. *Space Sci Rev* 128, 221–240 2007
18. Keller, H., U., et al., OSIRIS – The Scientific Camera System Onboard Rosetta, *Space Sci Rev* 128, 433-506, 2007
19. Glassmeier, K., *et al.* RPC-MAG, The Fluxgate Magnetometer in the ROSETTA Plasma Consortium. *Space Sci Rev* 128, 649–670, 2007
20. Auster, H.U., et al., The non-magnetic nucleus of comet 67p/Churyumov–Gerasimenko, Science 349, 6247, 2015
21. Fulle, M. et al, The dust-to-ices ratio in comets and Kuiper belt objects, MNRAS, 469, S45, 2017
22. Lorek, S., Gundlach, B., Lacerda P., Blum J., Comet formation in collapsing pebble clouds What cometary bulk density implies for the cloud mass and dust-to-ice ratio, A&A, 587, A128, 2016
23. Deshapriya, J. D. P., Exposed bright features on the comet 67P/Churyumov–Gerasimenko: distribution and evolution
24. Filacchione G. et al., Exposed water ice on the nucleus of comet 67P/Churyumov-Gerasimenko, Nature, 529, 368-372, 2016
25. Fornasier, S. et al., Rosetta's comet 67P/Churyumov-Gerasimenko sheds its dusty mantle to reveal its icy nature, Science, 354, 1566-1570, 2016.
26. Groussin, O. et al., Gravitational slopes, geomorphology, and material strengths of the nucleus of comet 67P/Churyumov-Gerasimenko from OSIRIS observations, A&A, 583, A32, 2015
27. Pätzold, M., Andert, T., Hahn, M., et al. A homogeneous nucleus for comet 67P/Churyumov–Gerasimenko from its gravity field, Nature, 530, 63, 2016

28. Fulle, M., Della Corte, V., Rotundi, A., et al. Comet 67P/Churyumov–Gerasimenko preserved the pebbles that formed planetesimals, Monthly Notices of the Royal Astronomical Society, 462, S132, 2016
29. Fulle, M. Blum, J., Rotundi, A., Gundlach, B., Güttler, C., Zakharov, V., How comets work: nucleus erosion versus dehydration, MNRAS 493, 4039, 2020
30. Gundlach, B., Fulle, M., Blum, J., On the activity of comets: understanding the gas and dust emission from comet 67P/Churyumov-Gerasimenko's south-pole region during perihelion, MNRAS 493, 3690-3715, 2020

ACKNOWLEDGEMENTS

B.G and J.B. thank the Deutsches Zentrium für Luft- und Raumfahrt (DLR) for continuous support and the Deutsche Forschungsgemeinschaft for their support under grant Bl 298/24-2 in the framework of the Research Unit FOR 2285 "Debris Disks in Planetary Systems". OSIRIS was built by a consortium led by the Max-Planck-Institut fur Sonnensystemforschung, Goettingen, Germany, in collaboration with CISAS, University of Padova, Italy, the Laboratoire d'Astrophysique de Marseille, France, the Instituto de Astrofisica de Andalucia, CSIC, Granada, Spain, the Scientific Support Office of the European Space Agency, Noordwijk, The Netherlands, the Instituto Nacional de Tecnica Aeroespacial, Madrid, Spain, the Universidad Politechnica de Madrid, Spain, the Department of Physics and Astronomy of Uppsala University, Sweden, and the Institut fur Datentechnik und Kommunikationsnetze der Technischen Universitat Braunschweig, Germany. The support of the national funding agencies of Germany (DLR), France (CNES), Italy (ASI), Spain (MEC), Sweden (SNSB), and the ESA Technical Directorate is gratefully acknowledged. Those authors part of the VIRTIS and GIADA teams wish to thank the Italian Space Agency (ASI, Italy) contract no. I/024/12/2 and Centre National d'Etudes Spatiales (CNES, France) for supporting their contribution. This research has made use of the scientific software shapeViewer (www.comet-toolbox.com). Video rendering was powered by PRo3D, a viewer for the exploration and analysis of planetary and smaller body surface reconstructions. It was developed by VRVis Zentrum für Virtual Reality und Visualisierung Forschungs-GmbH in close collaboration with JOANNEUM RESEARCH and Imperial College London. Please see http://pro3d.space for more details

Author Contributions

Identification of the skull-top crevice ice and other touchdown points made by LOR. Paper Lead writer is LOR. Contributions to methods & supplementary sections was performed by LOR, PH, SF, HVH, GF, AR, MC, JB, BGu, AR, MdPCP & GP. The ROMAP & RPC-MAG data analysis performed by PH, KHG & UA. The compressive strength & Volume filling analysis was performed by JB & BG. The OSIRIS image analysis was performed by LOR, SF & HVH. The VIRTIS data analysis was carried out by GF, AR, MC & FC. The Skull-top crevice Ice & dust analysis carried out by AR, DB, MK, OG, NO. The OSIRIS Image processing was performed by SF, HVH, GK, CT & HS. Trajectory data analysis was performed by BGr, LOR, RA, PH, JBV, CT & HS. The Shape model support and analysis given by LJ, JBV, RA, MdPCP & GP. Figures (in support of analysis) generated by LOR, PH, RA, JB, BGu, SF, HVH, GF, AR & MC. All authors have participated in the review of the paper & its contents.

Data Availability

The datasets generated during and/or analysed during the current study are available from the corresponding author on reasonable request. All OSIRIS images can be directly obtained from the ESA Planetary Science Archive (psa.esa.int).

Additional Information

- **Supplementary Methods** are available for this paper. In particular we would like to highlight the significance of the animated supplementary images & movies we provide in understanding better the imagery in our paper.
- Correspondence and requests for materials should be addressed to Laurence O'Rourke (lorourke@esa.int)
- Reprints and permissions information is available at www.nature.com/reprints

Methods Section

1. Spectral modelling & OSIRIS estimation of the water ice content for the "skull" boulder : The normal albedo presented has been evaluated from the photometricly corrected images using the shape 7S model with 12 million facets[31] and the Hapke model[32] parameters (Table 4 of [33]) from resolved photometry in the orange filter centered at 649 nm.

We assume that the phase function at 649 nm also applies at the other wavelengths[25]. The flux of a region of interest (ROI) in each of the 3 filters has been integrated over 3-pixel-wide, square boxes. We attempt to reproduce the spectral behavior and the normal albedo of the ice-rich patches by obtaining synthetic spectra of areal mixtures (spatially segregated) of the comets dark terrain (DT), derived from areas nearby the boulder with water ice:

$$R = \rho \times R_{\mathrm{ice}} + (1 - \rho) \times R_{\mathrm{DT}} \qquad (1)$$

where R is the reflectance of the bright patches, R_{ice} and R_{DT} are the reflectance of the water ice and of the comet dark terrain, respectively, and ρ is the relative surface fraction of water ice or frost.

We produce areal mixture models in view of the absence of reliable and relevant optical constants for the dark material needed to run more complex scattering models, and in view of the absence of clear absorption features in the wavelength range covered by the OSIRIS observations helping in constraining the nature of the materials and the grain size of the components in models. The water ice spectrum was derived from Hapke modeling of optical constants[34] using a grain size of 30 and 100 μm. In fact, the typical

size for ice grains on cometary nuclei was found to be of few tens of micrometers[35,36,37].

We also attempt to use models with larger water ice grains (up to 1000 and 2000 microns), but these models gave a worse spectral match and a lower chi-squared fit. The models that best fit the maximum absolute reflectance observed on the bright patch on the skull boulder are areal mixtures of the average cometary dark terrain (DT) enriched with 46.4-47.4% of water ice (Fig 3d, Extended Data Table 1) with grains size=30-100 μm. A further analysis is provided in Supplementary Methods.

2. VIRTIS Data Analysis : The best viewing opportunity for VIRTIS-M[38] of Philae Touch-Down 2 (TD2) site occurred on 14th June 2016 between 10:51:12 and 11:35:31 UTC when the Rosetta spacecraft was at a distance of 27.3 km from 67P and the solar phase angle was 57°.

During this period of time the VIRTIS-M instrument acquired a visible hyperspectral cube (acquisition V1_00424522185.QUB) by collecting 133 consecutive slit images of the surface with a spatial resolution of about 6.5x10 m (along slit x scan). Each slit image was acquired with an integration time of 16 s and a repetition step time of 20 s while the Rosetta spacecraft was maintaining nadir pointing. At each step the internal scan mirror is rotated by an angle of 250 μrad (corresponding to one IFOV) to achieve an angular scan of about 1.9° in 133 steps. Consecutive slits are not completely connected among them being separated by about 13 meters.

The resulting hyperspectral image of the Abydos region shown in Fig 3b has a scale of 1.66 km (slit width) by 0.86 km (scan length). The position of the cracked boulder on the TD2 site has been identified close to pixels at line=1, samples=163-168 and

appears located at the edge of the FOV (see Fig.3b, panel b2 - blue box). According to reconstructed geometries computed on SHAP7 digital model and including the current best estimate of the errors, the centres of these pixels are offset by a minimum of 25 to a maximum of 58 m with respect to the reference position of TD2. The identification of the TD2 location on VIRTIS image is therefore not fully certain due to the limited spatial resolution and position of the pixels on the edge of the VIRTIS image.

Due to the coarse spatial resolution, VIRTIS-M is not able to resolve the cracked boulder whose exposed bright area is of about 0.5 m^2 while the pixel area is 65 m^2. Moreover, due to the instrumental point spread function[39,40] FWHM (<500 μrad) and to the uncertainty on the position of the TD2 site, we are averaging the signal of the candidate TD2 area taken on 6 contiguous pixels where higher reflectance and blueing is observed.

The average reflectance spectrum of the TD2 pixels is shown in Extended Data Fig. 4a and compared with an average collected on nearby pixels (line=2, samples=163-168) as a reference for an adjacent non-icy terrain (Extended Data Fig. 4b). The analysis of the spectral slope measured on the two regions of interest gives a value of 2.39 and 2.59 1/μm for the cracked boulder pixels (blue curve) and nearby dark terrain (red curve), respectively. These values correspond to a spectral slope difference of Δ=0.20 1/μm. This difference is equivalent[41] to a water ice abundance of 0.1% in areal mixing (Extended Data Fig. 4c).

The dimension of the bright area on TD2 has been constrained to about 3.5 m^2 on OSIRIS high resolution images, of which about 1 m^2 made of exposed water ice in areal mixing (where water ice and dust are thermally not interacting therefore less energy is

available for sublimation). Our analysis shows that VIRTIS is missing the TD2 location by about one line and that the signal is harvesting the tail of the optical point spread function. As a consequence of this, we are collecting about 20% of the photons coming from the water ice patch on TD2 site. This means that the water ice abundance of 0.1 ± 0.04 % previously estimated is likely five times larger leading to 0.5± 0.2% . Scaling this value for the total area of 253 m^2 on 6 pixels, the water ice rich spot corresponds to an area of about 1.25 ± 0.5 m^2, in agreement with OSIRIS findings.

3. ROMAP and RPC-MAG data analysis : The tri-axial lander magnetometer ROMAP and orbiter magnetometer RPC-MAG were operating during the descent, landing and rebound phase with a sampling rate of 1 Hz. Extended Data Fig. 5 shows the measurements of both instruments for the interval around TD2. In order to use magnetic field measurements for flight dynamics reconstructions, reference measurements are necessary to separate between external events in the background magnetic field (e.g. magnetic wave activity as seen in the RPC-MAG observations in Extended Data Fig. 5) and changes caused by the spacecraft dynamics or operation (e.g. rotation change or boom movements). In this case the RPC-MAG orbiter instrument was used as background field reference to be able to reconstruct the Philae dynamics.

A rotation of the lander along an arbitrary axis relative to the background magnetic field causes an apparent rotation of the magnetic field vector observed by the lander relative to the orbiter reference. This causes the 3D quasi-sinusoidal modulation of the ROMAP measurements relative to the RPC-MAG measurements visible in Extended Data Fig. 5. A time-dependent rotation matrix between these two 3D observations can therefore be calculated to describe the attitude of the lander relative to the orbiter. This

information can then in theory be used to derive a set of time-dependent quaternions giving the absolute attitude of the lander.

A statistical analysis has to be used to accurately determine the absolute attitude to account for small deviations between the orbiter and lander measurements caused by noise and plasma phenomena (for detailed description[16]). In this case only a minimum amount of data points is available due to the low 1 Hz sampling rate and relatively fast changes in lander dynamics. Hence, a simplified analysis as introduced by Heinisch et al.[16] for the reconstruction of the rotation rate during descent was used to estimate the average lander rotation rate between the individual surface contacts (see Extended Data Table 2). Instead of determining the total absolute lander orientation this method is based on determining only the orientation of the lander rotation axis, which allows the lander magnetic field observations to be transformed into a temporary coordinate system in which one magnetic axis remains stable (i.e. the field along the rotation axis) and only the two remaining axis show a modulation. This modulation relative to the orbiter reference measurements can easily be determined and results directly in the lander rotation frequency as explained by Heinisch et al. [16]

A rotation of the magnetometer boom relative to the lander creates a characteristic signature (as can be seen around 17:25:30 in Fig. 2a and Extended Data Fig. 5) in the magnetic field caused by the displacement of the ROMAP sensor relative to the static lander bias field[17]. The shape and duration of this signature allows to constrain the acceleration acting on the lander perpendicular to the boom rotation axis i.e. along the lander z-axis. The other touchdowns[1,15] were used as reference to determine the direction

and timing and gain a qualitative insight on the magnitude (see supplement for more details)

4. Philae Lander Dynamics at Touchdown 2c point only : This section covers the dynamics at the TD2c point only where the ice was compressed by the Philae balcony and SD2 tower. The full dynamics that took place through all four TD2 points (TD2a-TD2d) are described in the Supplementary Methods and summarized in Extended Data Table 2.

After hitting the dust wall (TD2b) at 17:24:53±1s, Philae continued for an additional (30±1) s and (3.76±0.23) m in the horizontal direction and only approximately (0.50±0.18) m in the vertical direction, until 17:25:24 UTC where the next ROMAP boom movement was then detected (TD2c) – See Fig. 2a. This translated to a horizontal velocity of (0.125±0.013) m/s, a vertical velocity of (0.017±0.006) m/s and a kinetic energy of (0.771±0.179) J. Combined with the rotational energy this results in a total kinetic energy before TD2c and after the dust wall was hit at TD2b of (1.028±0.197) J. In total, the contact with the dust wall prior to TD2c dissipated (0.817±0.377) J of the kinetic energy of the lander.

The TD2c contact duration is linked to the ROMAP boom which showed an upwards movement at 17:25:24±1s continuing until approximately 17:25:27±1s (Fig. 2a, Extended Data Fig. 5). At 17:25:27±1s the boom started to move downwards away from the lid, meaning that the acceleration of the lander had stopped or reversed. The change at 17:25:27±1s is considered the end position of the stamping in TD2c because the geometry from the deceleration of Philae during stamping causes an upwards deflection of the boom which is what was observed. This resulted in a duration of 3±1s for the

stamping/compression of the ice (see Fig. 2a, 2b, 2c) and the animation in Supplementary Fig. 1.

The outgoing horizontal velocity is estimated to be zero as the stamping stopped the forward motion. The outgoing vertical velocity after the stamping is estimated to have a lower bound of (0.073±0.01) m/s while the energy loss at TD2c caused by the stamping is estimated to be (0.671±0.297J).

5. Estimating the surface area & depth of the ice impression : The images used in the data analysis are provided from numerous epochs and distances from the comet. The pixel resolution linked to distance ranged from 0.16m/pixel in May 2016 when the spacecraft was at 8.5km from the crevice, to 0.13m/pixel at a distance of 7km in June 2016, to 0.049m/pixel at the closest distance reached on 2nd September 2016 at 2.63km. The pixel size in Extended Data Fig. 2 for both pre- and post-landing images was 0.15m/pixel as the images were taken at an equivalent distance (8km) to the crevice. The pixel size used for the OSIRIS and VIRTIS measurements in Fig. 3a, 3b3 on June 14th 2016 was 0.49m at a distance of 26km from the crevice.

Image analysis relied primarily on cross-correlating multiple images to determine accurate estimates of heights and width of different boulder features. The lower the resolution the greater the error bar as it became difficult to determine where the edge of a feature actually started or ended due to the greater coverage of the pixel. The error bar is therefore linked to the pixel resolution achievable in the image analysis.

A lower limit of 0.2208m^2 has been estimated for the area of ice compressed by Philae in the TD2c position. Only two Osiris images (21st August 19:19, 24th August 2016 19:39 –

Figs. 1f, 2c) provide a clear, albeit angled, view of the ice in the compression. The full width of the ice impression could not be estimated therefore due to lack of direct visibility. It was feasible however to use both these images as well as another from the 2nd September 2016 19:59 in Fig. 3e (which provides an edge-on-view of the ice impression) to obtain a lower limit measurement of the length of the sides of the Philae balcony that made the impression. The estimate is a combination therefore of the actual area of the Philae balcony matching these lengths plus the area of an arc matching the remainder of the angled visible ice. The image from the 2nd September also provided a clear measurement 0.246 ± 0.049m to be made of the depth of the ice in the compressed zone.

Figs. 1d, 2b and 3e (same images) were taken on 2nd September 2016 at the closest distance (2.63km) to the nucleus surface achieved by Rosetta during the mission and provide therefore the highest resolution. This image, which was the famous Philae discovery image, provides a clear high resolution view of the edge of the compressed ice region in TD2c. The sun illumination in this image is equivalent to the illumination observed on 6th August 05:52 and allows to conclude that while the sunlight was gradually moving down the crevice, it had not yet arrived at the compressed region thus the stamped edge lies in shadow with the exposed ice further back in the crevice creating a back-light effect. This edge-on view allows an accurate measurement of 0.246 ± 0.049m to be taken of the depth of the compressed region. In that respect, the one image showing Philae resting on the surface of the comet also provides the key input measurement for this paper (Fig. 1d).

6. Deriving the compressive strength and porosity of cometary boulder ice

The model we use : To derive material properties for the cometary boulder from our findings we consider a hierarchical setup of the interior structure of the boulder assuming the dust and ice grains is concentrated in larger units ("pebbles"), which themselves are clustered together to make up the boulder[7]. Thus, the boulder itself is a kind of "rubble pile" and possesses pore space on two length scales, the microscopic and the pebble-size length scale. Comparisons between our model and others addressing the basic building blocks of the internal material of the comet can be found in [10,11,7,30, + Herique et al 2019] and are not dealt with any further in this paper.

Compressive strength estimates : As the incoming trajectory of Philae at TD2c with respect to the surface normal shows, Philae lost a total kinetic energy of $\Delta E = 0.671 \pm 0.297$ J due to compression ("stamping") of the surface material of comet 67P. The vertical component of the incoming motion of Philae resulted in the compaction of the porous cometary matter. The characteristic stress required for stamping is determined by the compressive strength P_{C} of the material. With the depth and minimum area of the stamping impression Philae made estimated (see main text) to be $h = 0.246 \pm 0.049$ m and $A_{\mathrm{Min}} = 0.2208$ m^2, respectively, a minimum volume of $V_{\mathrm{Min}} = A_{\mathrm{Min}} \cdot h = 0.054$ m^3 was displaced during stamping.

We can make a first, crude, estimate of the compressive strength by assuming that the compressed volume is at least V_{Min} and that the compressive strength is a constant material value, i.e., is independent of the compressional state of the matter. In reality, a much larger volume than V_{Min} is affected by the impact of Philae and P_C is a strong function of the porosity (see below). However, we can state that $P_C < \frac{\Delta E}{V_{\mathrm{Min}}} = 12$ Pa is

required to account for the observed material compression and energy loss of Philae. It should be noted that this upper limit for the compressive strength of 67P's surface material is model independent and based on firm measurements (this paper).

Compressive strength link to volume filling factor : The compressive strength is not a constant material value, but rather depends on the volume filling factor (fraction of total volume filled by material), Φ, in a characteristic way[13,42,43]

$$P_C(\Phi) = p_m \left(\frac{\Phi - \Phi_1}{\Phi_2 - \Phi}\right)^{\Delta'},$$

with Φ_1 and Φ_2 being the formal lower and upper limits of the volume filling factor for which $P_C(\Phi_1) = 0$ and $P_C(\Phi_2) \to \infty$, respectively.

Experiments showed[13,42,43] that Φ_2 is in the range of $\Phi_2 \approx 0.3 - 0.7$, depending on the particle properties, such as grain size, grain-size distribution, grain shape, and the mode of compression. The value of Φ_1, which has no physical meaning and is merely a fit parameter, ranges[43] between $\Phi_1 = 0.05$ and $\Phi_1 = 0.35$. The factor p_m is the characteristic compressive strength and Δ' describes the logarithmic range of stresses in which compression takes place, i.e., most compression happens in the interval $\left(10^{-\Delta'} \cdot p_m, 10^{+\Delta'} \cdot p_m\right)$.

Schräpler et al.[43] showed that this relation also holds for a wide range of particale sizes covering from loose granular ensembles of dust aggregates (the "pebbles" in our notation) to others of a more homogeneous assemblage. They also showed that $= 1.3$ is an appropriate value for all kinds of grain and pebble sizes. Pebble assemblages possess characteristic compressive strengths of p_m,1 $\approx 6.1 \times 10^{-2}$ Pa for pebbles with 1 mm

radius and p_m,2 ≈ 4.7 × 10^{-3} Pa for pebbles with 1 cm radius (for the heterogenous case – as is our model), whereas sub-micrometre-sized particles in a more homogenous structure are compressed with $p_m \approx 10^4$ Pa. The schematic functional dependence of the volume filling factor on compression for our model is shown in Extended Data Fig. 6c

Volume filling factor applied to the cometary boulder interior (TD2c): To estimate the volume filling factor, and therefore the porosity, we need to take into account the manner in which the pebbles assemblage compacts when the boulder interior is formed. The different ways in which this can be happening can vary as touched upon briefly in the Supplementary section whether it occurs at initial cometary formation or long afterwards as the result of cometary dynamical events. The resulting packing fraction of the pebble assemblage can be defined in these scenarios by random loose packing (RLP), which means[44] ≈ 0.55, if inter-pebble friction is strong[45]. Due to the nature of the pebbles as dust/ice aggregate, a strong frictional interaction is expected.

The maximum random packing density is random close packing (RCP), or[44,45] ≈ 0.64. Thus, Philae's energy was dissipated by the compaction from RLP towards RCP (see Extended data Fig. 6c). The total compressed volume must be larger than the displaced volume, V_{Min}, to make room for the displaced material (Extended Data Fig. 6a and b). Assuming that the overall compressed volume is $V_{\mathrm{Eff}} = \eta V_{\mathrm{Min}}$ and that the increase in volume filling factor from initially $\Phi_{\mathrm{Min}} = \Phi_{\mathrm{RLP}}$ to Φ_{Max} is identical everywhere inside this volume, the volume scaling factor can be derived as $\eta = \frac{\Phi_{\mathrm{Min}}}{\delta\Phi}$, with $\delta\Phi = \Phi_{\mathrm{Max}} - \Phi_{\mathrm{Min}}$ We can calculate the energy dissipated by Philae's stamping motion (in z direction), $\Delta E = 0.671$ J to

$$\Delta E = \int_{V_{\mathrm{Eff}}+V_{\mathrm{Min}}}^{V_{\mathrm{Eff}}} P_C \mathrm{d}V$$

$$= A\int_0^h P_C \mathrm{d}z$$

$$= Ap_m \int_0^h \left(\frac{\Phi(\mathrm{z}) - \Phi_1}{\Phi_{\mathrm{RCP}} - \Phi(\mathrm{z})}\right)^{\Delta'} \mathrm{d}z$$

$$= Ap_m \int_{\Phi_{\mathrm{Min}}}^{\Phi_{\mathrm{Max}}} \left(\frac{\Phi - \Phi_1}{\Phi_{\mathrm{RCP}} - \Phi}\right)^{\Delta'} \frac{\mathrm{d}z}{\mathrm{d}\Phi} \mathrm{d}\Phi$$

$$= \frac{V_{\mathrm{Min}} p_m}{\delta\Phi} \int_{\Phi_{\mathrm{Min}}}^{\Phi_{\mathrm{Max}}} \left(\frac{\Phi - \Phi_1}{\Phi_{\mathrm{RCP}} - \Phi}\right)^{\Delta'} \mathrm{d}\Phi \ ,$$

Equation (1)

in which we use the approximation $\Phi(\mathrm{z}) = \Phi_{\mathrm{Min}} + \frac{z}{h}\delta\Phi$ and $\frac{\mathrm{d}z}{\mathrm{d}\Phi} = \frac{h}{\delta\Phi}$, with h = 0.246 m and A = 0.2208 m^2 being Philae's intrusion and stamping cross section.

Applying Eq. 1 (see also supplementary Table 1) with the nominal values $p_m \approx 10^{-2}$ Pa, $\Phi_{\mathrm{Min}} = \Phi_{\mathrm{RLP}} = 0.55$, $\Delta' = 1{,}3$ and $\Phi_1 = 0.05$ shows that $\Phi_{\mathrm{Max}} \approx \Phi_{\mathrm{RCP}}$ and, thus, $\eta = 6.1$ and $V_{\mathrm{Eff}} = 0.33$ m^3.

It should be noted that the volume filling factor assumed in the above calculation, $\Phi = \Phi_{\mathrm{RLP}} \approx 0.55$, is that of the pebble assemblage. The pebbles themselves consist of sub-µm-sized dust/ice particles so that they possess internal porosity, which can be expressed by their inner volume filling factor $\Phi_{\mathrm{pebble}} \approx$ 0.33-0.58, depending on the type of compression experienced by the pebbles in the laboratory[42].

Taking the average of this range in volume filling factor of the pebbles, $\Phi_{\text{pebble}} = 0.455 \pm 0.125$, we get an overall volume filling factor of the boulder of $\Phi_{\text{boulder}} = \Phi RLP \cdot \Phi pebble = 0.25 \pm 0.07$, in good agreement with the values determined by Rosetta (see above).

REFERENCES NUMBERS CONTINUED FROM MAIN PAPER

31. Jorda, L. et al., The global shape, density and rotation of 67P/Churyumov-Gerasimenko from pre-perihelion Rosetta/OSIRIS observations. Icarus **277**, 257-278 (2016).

32. Hapke, B. et al, Bidirectional Reflectance Spectroscopy. 5. The Coherent Backscatter Opposition Effect and Anisotropic Scattering. Icarus **157**, 523-534 (2002).

33. Fornasier S., et al., Spectrophotometric properties of the nucleus of comet 67P/Churyumov-Gerasimenko from the OSIRIS instrument onboard the ROSETTA spacecraft. Astron. Astrophys **583**, A30 (2015).

34. Warren, S. G, Brandt, R.E., Optical constants of ice from the ultraviolet to the microwave: A revised compilation. J. Geophys. Res. **113**, D14220 (2008).

35. Sunshine, J.M. et al., Exposed Water Ice Deposits on the Surface of Comet 9P/Tempel 1. Science **311**, 1453-1455 (2006).

36. Capaccioni, F., et al., The organic-rich surface of comet 67P/Churyumov-Gerasimenko as seen by VIRTIS/Rosetta. Sci- ence **337**, a0628 (2015).

37. Filacchione, G., et al., The global surface composition of 67P/CG nucleus by Rosetta/VIRTIS Prelanding mission phase. Icarus **274**, 334-349 (2016).

38. Coradini, A., *et al.* VIRTIS: An imaging spectrometer for the Rosetta mission, *Space Sci Rev* 128, 529–559, 2007

39. Filacchione, G., On-ground characterization of Rosetta/VIRTIS-M. II. Spatial and radiometric calibrations, Review of Scientific Instruments, Volume 77, Issue 10, pp. 103106-103106-9 (2006).

40. Ammniito, E. et al., On-ground characterization of Rosetta/VIRTIS-M. I. Spectral

and geometrical calibrations, Review of Scientific Instruments, Volume 77, Issue 9, pp. 093109-093109-10, 2006

41. Raponi, A. et al, The temporal evolution of exposed water ice-rich areas on the surface of 67P/Churyumov-Gerasimenko: spectral analysis, MNRAS, Volume 462, Issue Suppl_1, p.S476-S490, 2016
42. Güttler, C. et al. , The Physics of Protoplanetesimal Dust Agglomerates. IV. Toward a Dynamical Collision Model, ApJ, Volume 701, Issue 1, pp. 130-141, 2009
43. Schräpler, R. et al., The stratification of regolith on celestial objects, Icarus, Volume 257, p. 33-46, 2015
44. Onoda, G.Y., Liniger, E.G., Random loose packings of uniform spheres and the dilatancy onset, Physical Review Letters, Volume 64, Issue 22, pp.2727-2730, 1990
45. Luding, S., Granular matter: So much for the jamming point, Nature Physics, Volume 12, Issue 6, pp. 531-532 2016.
46. Groussin, O. et al., The Thermal, Mechanical, Structural, and Dielectric Properties of Cometary Nuclei After Rosetta, Space Science Reviews, Volume 215, Issue 4, article id. 29, 51 pp., 2019

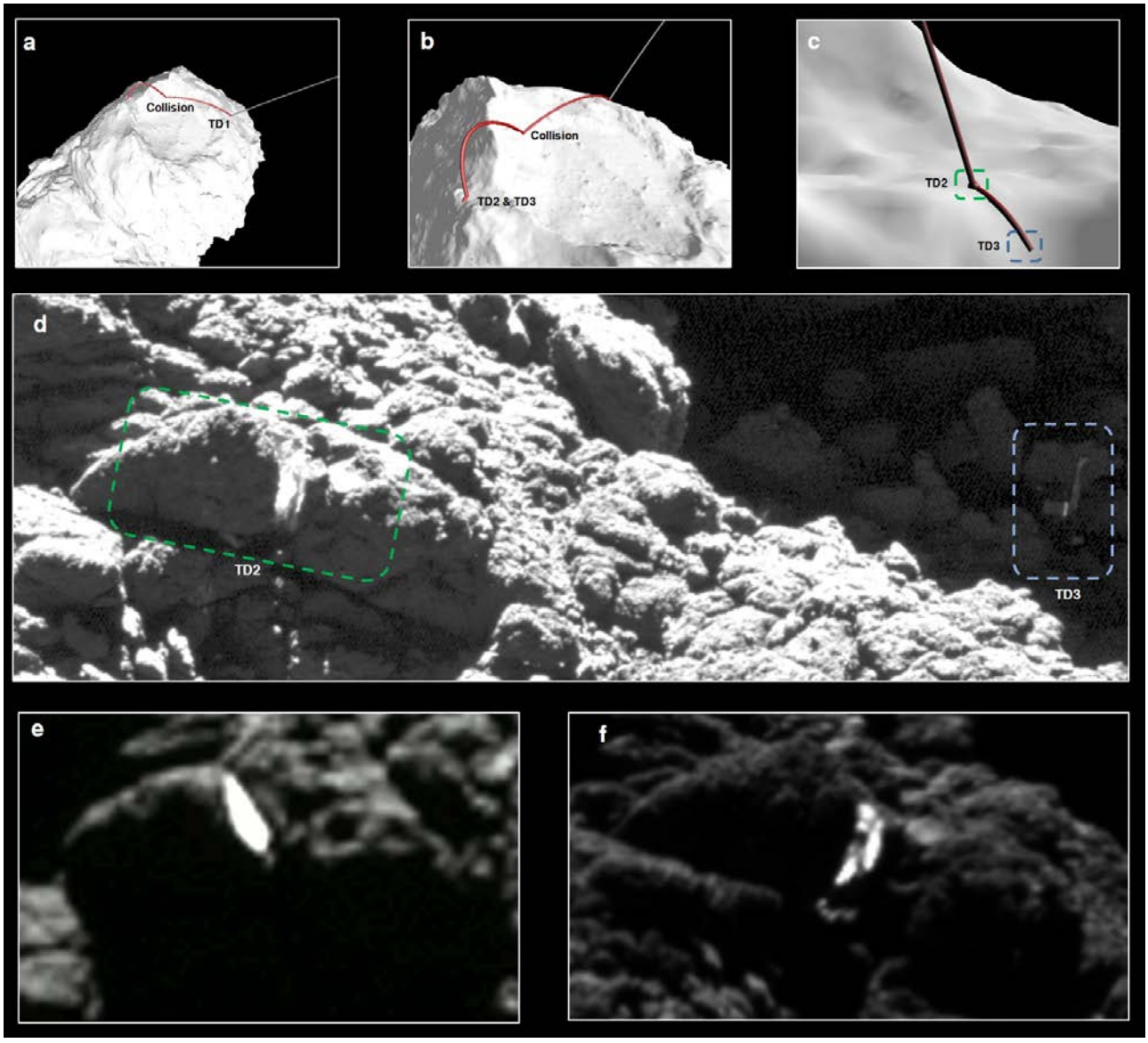

Fig. 1 – CAPTION TO BE UPDATED - Philae compresses ice in skull-top crevice and hides in plain sight.. (d) An overexposed OSIRIS Image (2nd Sept 2016 19:59 UT; 0.049 m/pixel) showing the skull-top crevice and the Philae lander hidden in the distant shadows

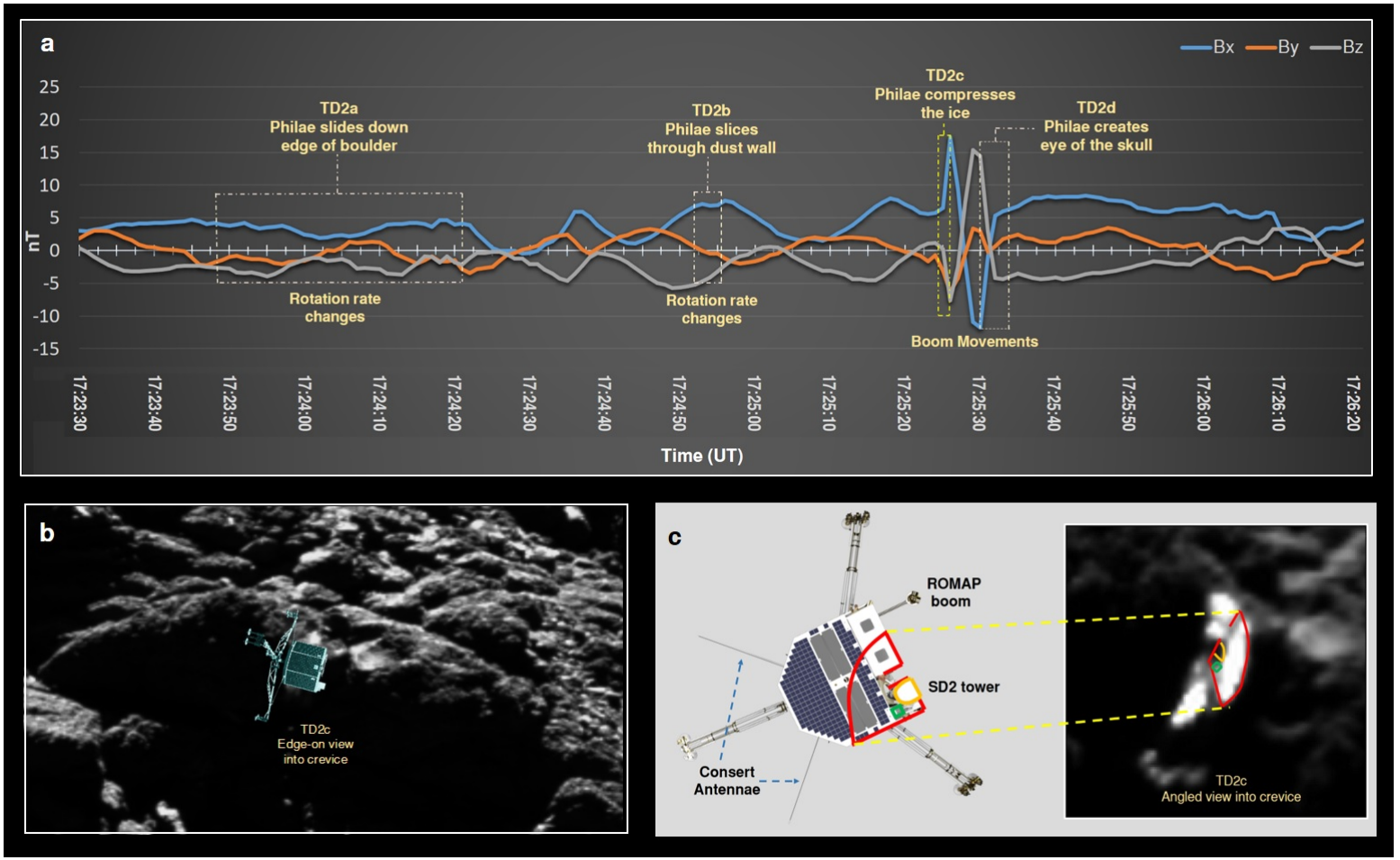

Fig. 2 – CAPTION TO BE UPDATED :

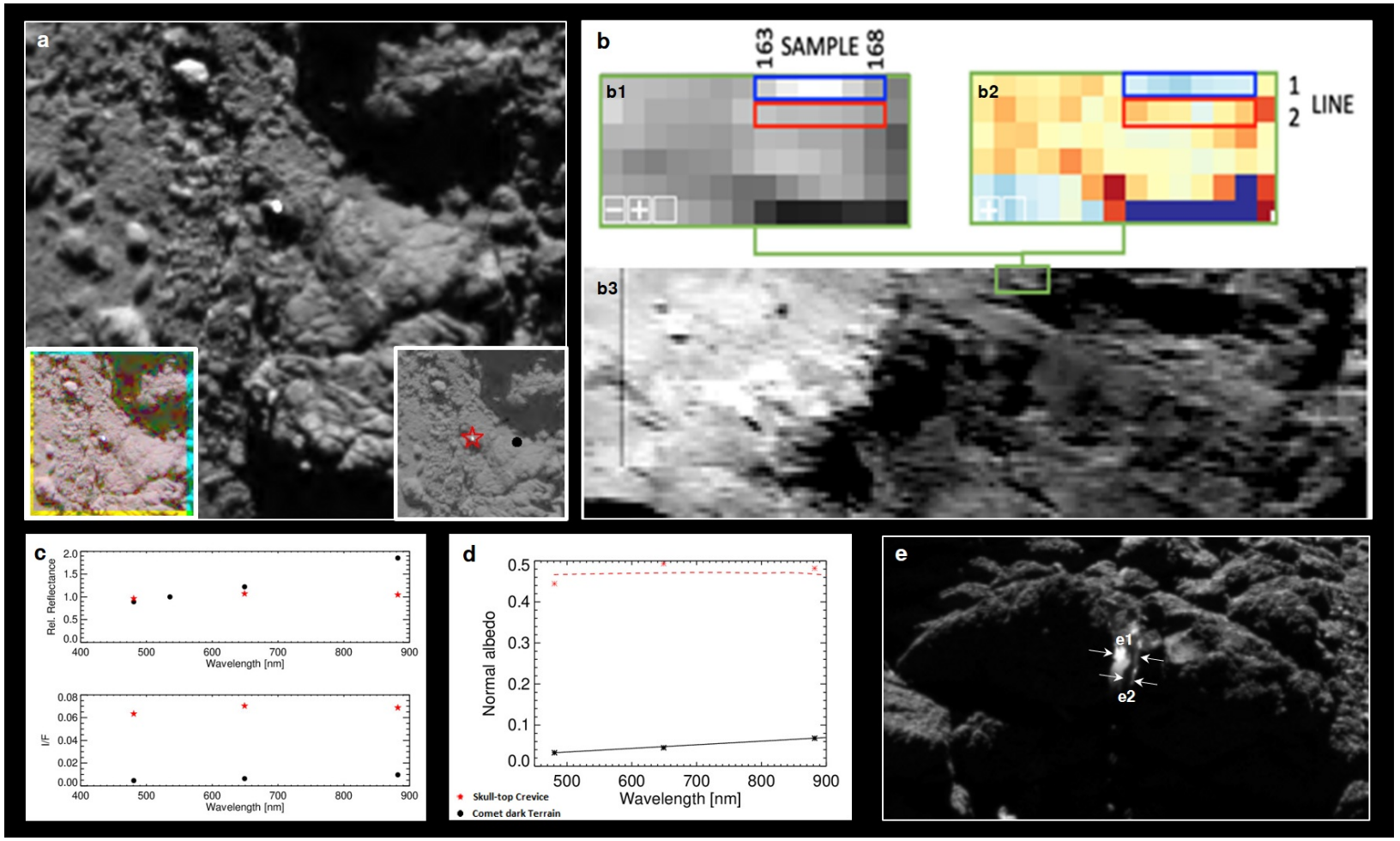

Fig. 3 – CAPTION TO BE UPDATED :

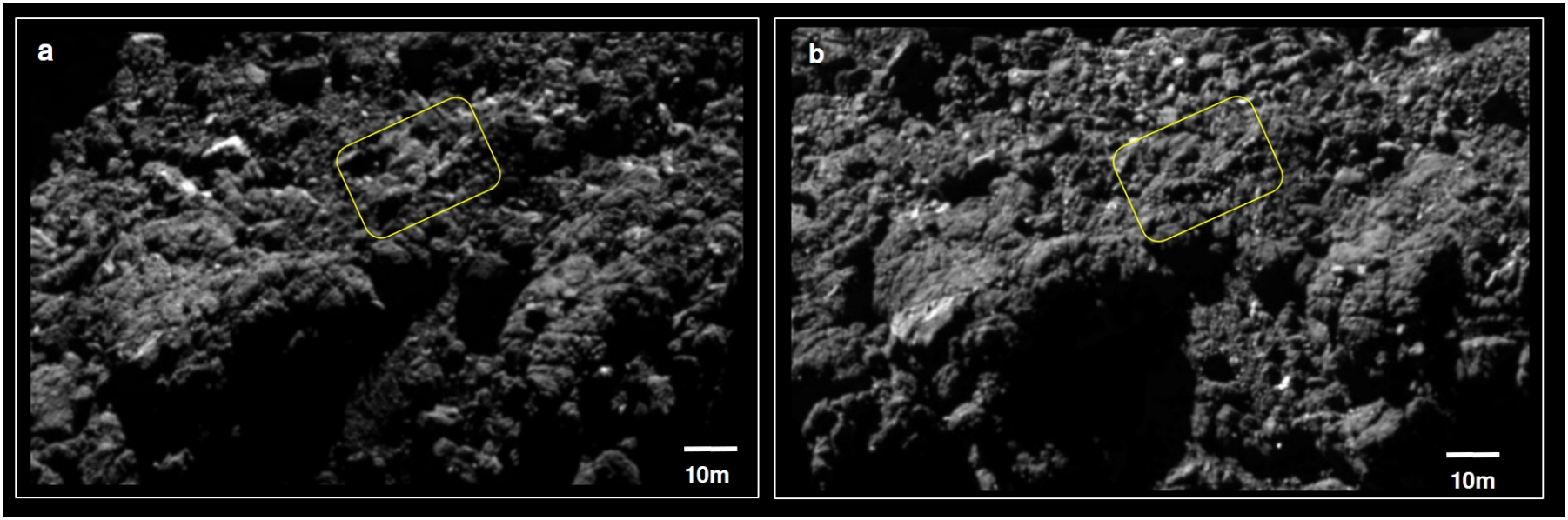

Extended Data Fig. 1 : Pre & post-landing image comparison. This figure compares the skull-top ridge location as it looked pre-landing and post-landing. **a** OSIRIS image of 22nd October 2014 (pre-landing) and **b** 14th May 2016 (post-landing). The yellow rectangle highlights the location of the skull-top boulders. Key differences between the images lie in the sun illumination and Rosetta orbital viewing geometry however the spacecraft distance is the same (8km). The Philae lander is highlighted with an arrow in the post-landing image. See Extended Data Fig. 5 for a detailed comparison between the skull-top boulder locations shown in the images.

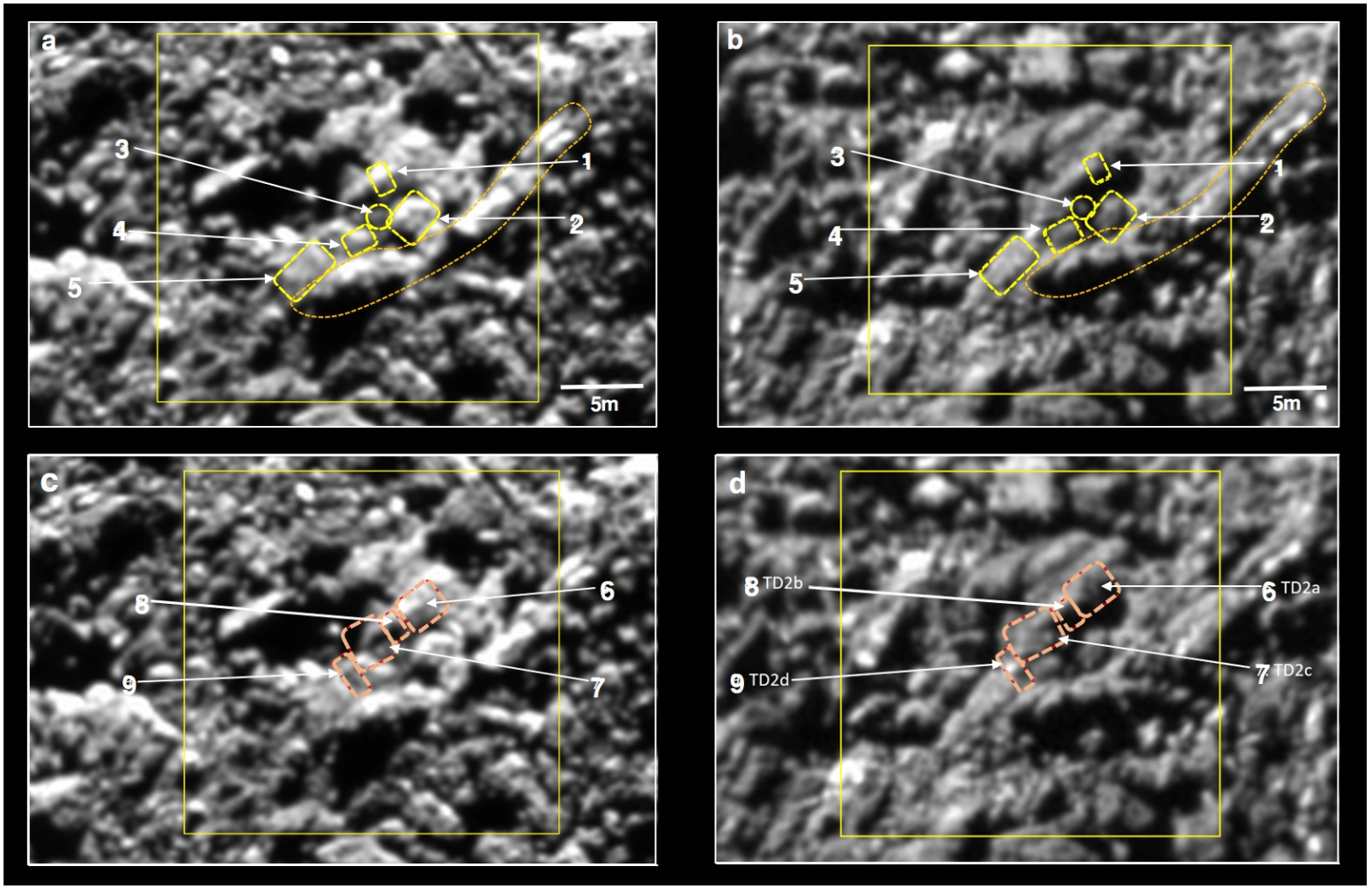
a
3
1
4
2
5
5m
b
3
1
4
2
5
5m
c
8
6
9
7
d
8 TD2b
6 TD2a
9 TD2d
7 TD2c

Extended Data Fig. 2 Analysis of pre & post-landing images. a & c : 22nd Oct 2014 **b & d** : 14th May 2016. Images **a** and **b** highlight five similarities (yellow dashes) between the images. Although viewing geometry & illumination differs, the same features are observed. Images **c** and **d** show differences (red dashes) between images. Points 6-9 in image **d** differ significantly with the same points in image **c** because they correspond to the 4 touchdown points (TD2a-2d). The boulders located above and to the left of the skull-top boulder region are located down in the Abydos valley.

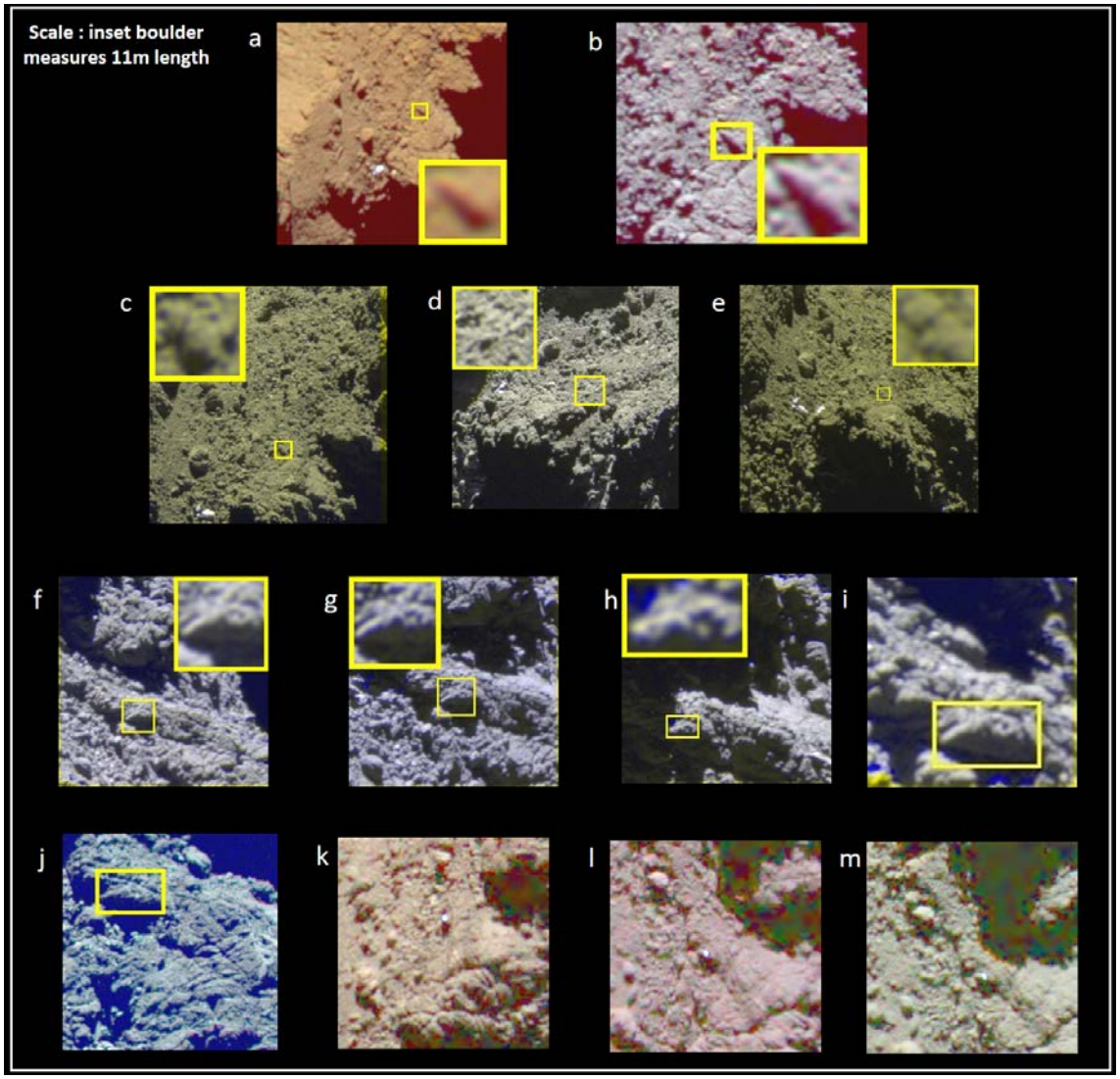

Extended Data Fig. 3 OSIRIS Colour composites of skull-top boulders Images **a** & **b** Pre-landing images of "skull-top" boulders (inset); RGB setting: "green"= F24 (480.7 nm), "red"= F22 (649.2 nm), "blue"= F16 (360.0 nm). Images **c-e** "skull-top" boulders observed December 2014; RGB setting: "green"= "red"= F22 (649.2 nm), "blue"= F24 (480.7 nm). Images **f-i** The "skull-top" boulders observed in March 2016; RGB setting: "green"= "red"= F22 (649.2 nm), "blue"= F24 (480.7 nm).. Images **j-m** Color composite of the "skull-top" boulders in early and mid-June 2016; RGB setting: "green"= F24 (480.7 nm), "red"= F22 (649.2 nm), "blue"= F16 (360.0 nm).

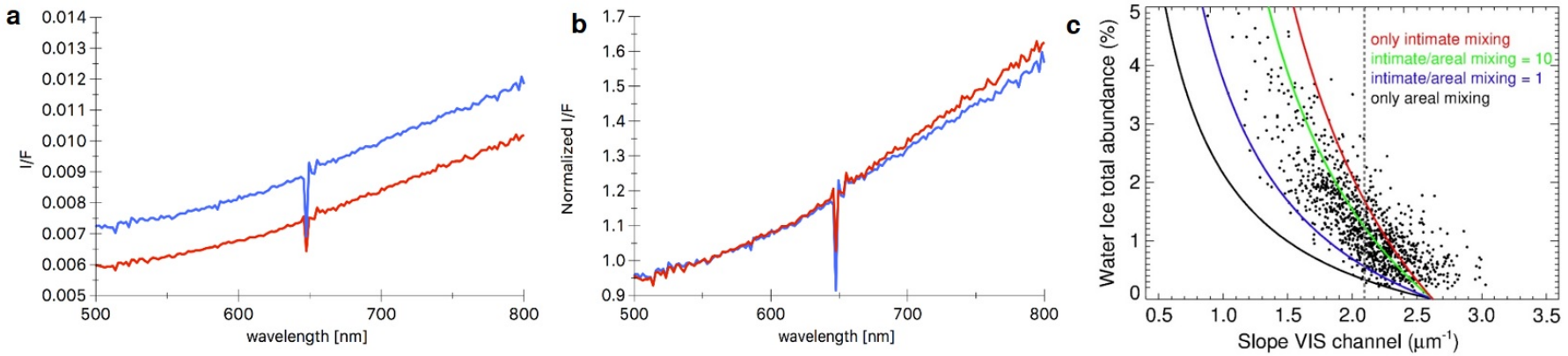

Extended Data Fig. 4 VIRTIS water ice analysis plots – Average I/F of skull-top boulder location (blue curve) and on the nearby dark terrain (red curve) before (plot a) and after (plot b) normalization at 550 nm. Plot c : theoretical abundance of water ice as a function of the spectral slope in the visible spectral channel[41]. Black dots and dashed lines indicate a water ice rich region observed by VIRTIS to calibrate the theoretical curves. The magenta x-axis values correspond to slope values scaled to the dark terrain unit viewing conditions (Fig 3b. panel b1 red box) for observation V1_00424522185.QUB.

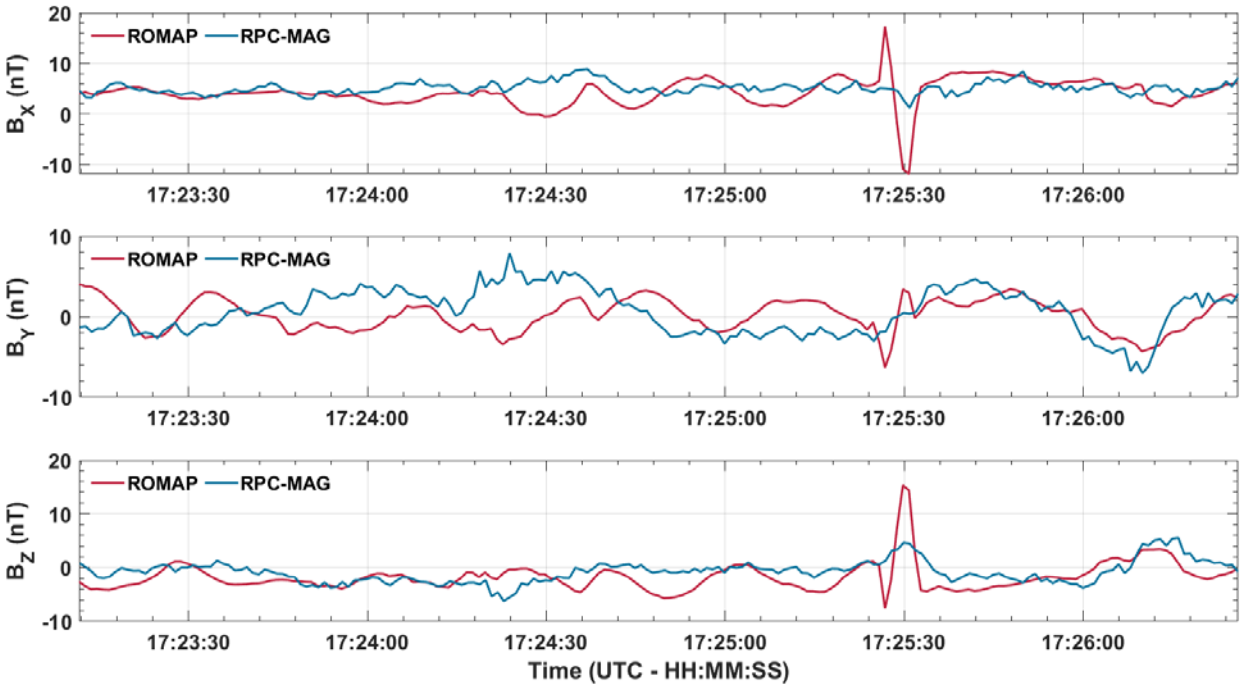

Extended Data Fig. 5 Combined ROMAP and RPC-MAG magnetic field and boom measurements. CAPTION TO BE UPDATED

The three components of the magnetic field observations are shown starting before TD2 at 17:23:00 UTC and ending shortly after the boom movement was detected. This figure also shows the concurrent orbiter RPC-MAG observations as reference.

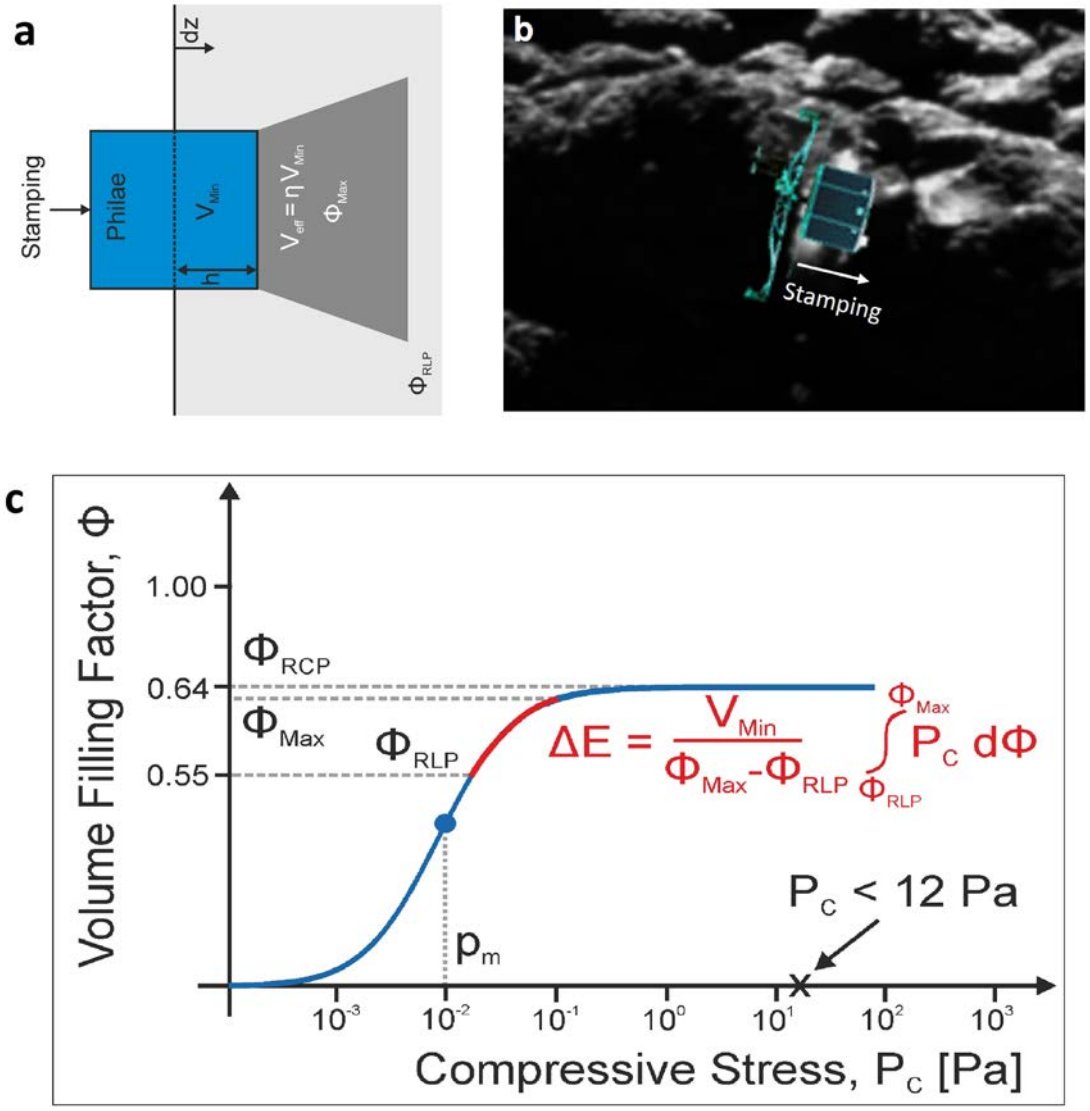

Extended Data Fig. 6 : CAPTION TO BE UPDATED

Acquisition time	Δ (km)	α (°)	Area (m^2)	ρ (30 μm)	ρ (100 μm)
2016-06-12T22:29:58	27.5	81.4	3.7	$28.8^{+5.8}_{-5.3}$%	$30.3^{+6.1}_{-5.5}$%
2016-06-14T10:30:32	26.7	54.0	3.5	46.4%	47.4%
2016-06-14T22:23:41	26.3	48.6	2.5	40.7%	43.0%

Extended Data Table 1 - Estimation of the water ice content of the bright spot observed at the crevice of the "skull" boulder on three separate observations by the OSIRIS instrument in mid June 2016. Δ: distance between the spacecraft and the comet surface, α: phase angle and ρ: water ice fraction. The 14th June 2016 10:30:32 image provides the highest value as the illumination into the crevice and viewing condition was the best of the three opportunities.

	TD2a (Initial Contact)	TD2b (Dust wall)	TD2c (Stamping)	TD2d (Dust compression)
Start Time (UT)	17:23:48±10s	17:24:53±1s	17:25:24 ±1s	17:25:30±1s
End Time (UT)	17:24:22±1s		17:25:27±1s	17:25:33±1s
Contact Time t (s)	30±10x	2±1	3±1	2±1
Incoming Kinetic Energy (J)	2.97±0.15	1.845±0.18	1.028±0.197	0.357±0.1
Outgoing Kinetic Energy (J)	1.974±0.18	1.028±0.197	0.357±0.1	0.10±0.02
Energy Loss (J)	1.342±0.33	0.817±0.377	0.671±0.297	0.257±0.12
Incoming Rotation Rate (mHz)	42.0±1.0	64.0±1.0	28±1.0	33±1.0
Outgoing Rotation Rate (mHz)	64.0±1.0	28±1.0	33±5.0	2±0.5
Incoming Vertical Velocity (m/s)	≈ −0.194	-0.034±0.008	-0.017±0.006	≈ 0
Incoming Horizontal Velocity (m/s)	≈ 0.098	0.109±0.011	0.125±0.013	≈ 0
Outgoing Vertical Velocity (m/s)	-0.034±0.008	-0.017±0.006	>+0.073 (after stamping)	≈ + 0.007
Outgoing Horizontal Velocity (m/s)	0.109±0.011	0.125±0.013	≈ 0	≈ 0.090

Extended Data Table 2 Philae lander dynamics through TD2a to TD2d Summary of the underlying values and results for TD2 including timing as described in the Methods (Philae Lander Dynamics at Touchdown 2c point only) and Supplementary Methods (Detailed Description of flight through TD2 from ROMAP/RPC-MAG Analysis)